# Development of a Smart Shoe for Building a Real-Time 3D Map

Luan V. Nguyen[a] and Hung M. La[b]
[a,b]Department of Computer Science and Engineering, University of Nevada, Reno, NV 89557, USA.
E-mail: luan@nevada.unr.edu; hla@unr.edu.

***Abstract*—Three dimensional (3D) mapping of environments has gained significant research interest over the last decades because of its important need for environmental modeling and monitoring. There are many successful research efforts in this field, and even it has been turned into commercial products such as Velodyne Lidar [1]. However, due to natural localization challenges, not much research for 3D mapping wearable sensor devices has been successfully reported. In this paper, we are interested in building a smart and wearable shoe which integrates multiple laser scanners and an inertial measurement unit (IMU) to build a 3D map of the environments. The proposed Smart Shoe can collect data and build a real-time 3D map during human walking. Such a smart shoe can support disabled people (blind people) to easily navigate and avoid obstacles in the environment. Additionally, this shoe can help firefighters quickly model and recognize objects in the fired and dark smoke buildings where the cameras may not be useful. The developed localization algorithm using IMU can output a smooth and accurate pose and trajectory of the human walking. This key importance of the shoe localization enables 3D mapping successfully while minimizing data registration error from the laser point cloud.**

**Keywords: Robotics, 3D Mapping, Real-time 3D Mapping Algorithms, SLAM.**

## I. Introduction

Three dimensional (3D) mapping of an unknown environment is open and interesting research since it has broad applications in environmental searching, exploring and monitoring [2], [7], [13], [17]. There are some successful research efforts in this field, and even it has been turned into commercial products such as Velodyne Lidar [1]. Integration of laser scanners or 3D LiDar sensor to build a 3D map of the environment is reported in [3], [11], [18], [21]. Their proposed 3D mapping systems integrated on mobile vehicle can work on a large scale of the environment, but they are not suitable for a device with normally worm such as our shoe in this paper. Besides, due to natural localization challenges [1], [4], [8], [19], not much research for 3D real-time mapping wearable sensor devices has been successfully reported.

It started from our observation of human motion gait to propose an idea for designing a smart shoe which is compact, comfortable and naturally wearable. There are some potential applications of the proposed shoe. For example, with 3D real-time mapping feature, the shoe can help visually impaired users improve their navigation capabilities. Besides, the proposed shoe can help firefighters quickly model and recognize objects in the fired and dark smoke buildings where the cameras may not be useful.

The smart shoe design with wearable sensor devices including laser scanners and inertial measurement unit (IMU) for 3D real-time mapping faces with several challenges. First, it requires a very compact design for the natural movement of foot, especially when walking fast, climbing up or down stairs, running or jumping. Second, in order to build a 3D map, accurately tracking position and orientation of a shoe is important [12], [15]. Finally, the swing of laser scanning devices during the foot's movement increases noise of collected data and reduces the accuracy of a 3D map.

To deal with these challenges, by utilizing the human gait motion, we first propose a simultaneous human foot motion localization algorithm to accurately and smoothly output the foot position. We then calibrate the laser scanning data with the foot's pose to enable a 3D mapping. This result can be a frame work for other applications of mobile wearable devices for 3D mapping in real-time not only the shoe.

The remaining of the paper is organized as follows. The next section presents an overview of the smart shoe design. Section III presents the real-time human foot motion localization scheme. The 3D mapping algorithm for the smart shoe is presented in Section IV. Section V presents experimental results to demonstrate the effectiveness of the proposed smart shoe. Finally, the conclusion and future work is discussed in Section VI.

## II. Overall Design of a Smart Shoe

### A. Design of a Smart Shoe

The smart shoe sketch is depicted in Fig. 1 and its components are presented in Fig. 2. Two Hokuyo laser

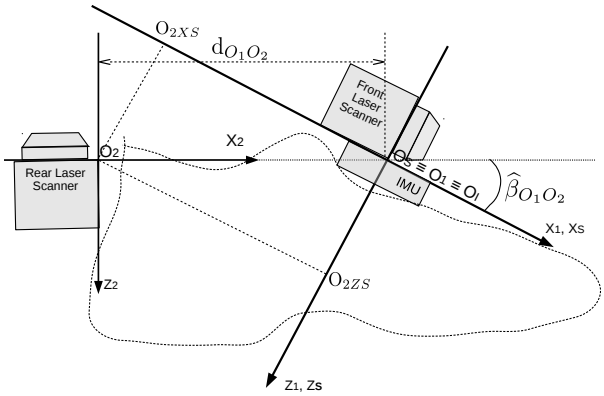


Fig. 1. A Smart Shoe design

scanners are mounted on the front and rear sides of the shoe. Due to different mounting locations, the lasers have different detected/scanned areas, detected distances, number of points per scanning, and the output result rate. In this

This work was partially supported by the University of Nevada Reno and the National Science Foundation under the grants: NSF-NRI-1426828 and NSF-Icorps-1535716.

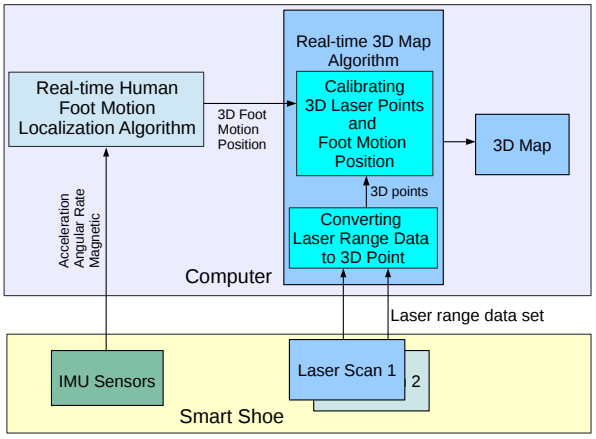


Fig. 2. A Smart Shoe Components

design, the shoe is considered as a rigid body frame [5] and includes three sub body frames: $LaserScanner1$, $IMU$, and $LaserScanner2$. The distance between two centers $O_1$ of $LaserScanner1$ frame and $O_2$ of $LaserScanner2$ frame is $d_{O_1O_2}$, and the axis $O_1O_2$ is parallel with the bottom of the shoe background. The body frame of $LaserScanner1$ is the same as the body frame of the shoe. Hence, $O_1$ is equivalent to $O_S$ of the $SmartShoe$ body frame center. The $IMU$ sensor is mounted under the Laser Scanner 1. We decided that the $IMU$ body frame is also the same as the $SmartShoe$ body frame. So the original center $O_I$ of $IMU$ body frame, $O_S$ of $SmartShoe$ body frame, and of course the $O_1$ of $LaserScanner1$ body frame are equivalent to, $O_S \equiv O_1 \equiv O_I$, as in Fig. 1. The angle rate of $IMU$ ($Roll$, $Pitch$, $Yaw$) during foot movement is also the angle rate of $LaserScanner1$ body frame and shoe body frame movement. The angle rate of $LaserScanner2$ frame movement is equal to ($Roll$, $Pitch$ + $\widehat{\beta}_{O_1O_2}$, $Yaw$) in which ($Roll$, $Pitch$, and $Yaw$) are the angle rates of $IMU$, $LaserScanner1$ and $SmartShoe$, respectively.

In this design, we assign the coordinate system of $SmartShoe$ body frame $(X_S, Y_S, Z_S)$ and $LaserScanner1$ body frame $(X_1, Y_1, Z_1)$ to be the same as $IMU$ inertial coordinate system $(X_I, Y_I, Z_I)$ as shown in Fig. 1. The Z axises in these body coordinate systems are down. The $X_1$, $X_I$, and $X_S$ are equivalent to $Roll$ angle axis of the shoe. The $Y_1$, $Y_I$, and $Y_S$ are equivalent to $Pitch$ angle axis of the shoe. And $Z_1$, $Z_I$, and $Z_S$ are equivalent to $Yaw$ axis of the shoe.

### B. Scanning Field of the Smart Shoe

The scanning field of this Smart Shoe is very crucial for the success of building a 3D map. Because one of important requirements of this Smart Shoe is to be able to scan a full $360^0$ above the background for a 3D map building (see Fig. 3). Missing any part of this half sphere can lead to the failure of a full 3D map. By observing a gait cycle of human foot motion (see Fig. 4), we discovered that the changing angle of the foot could help the shoe scan a maximum $5\pi/6$ of $Pitch$ angle above the background. This angle change depends on the walking speeds [20] [22]. Hence, by integrating two Laser Scanners on a shoe, the scanning field of the Smart Shoe may reach to a maximum covered angle of $5\pi/6$ in the $Pitch$ angle axis as can be seen in Fig. 3.

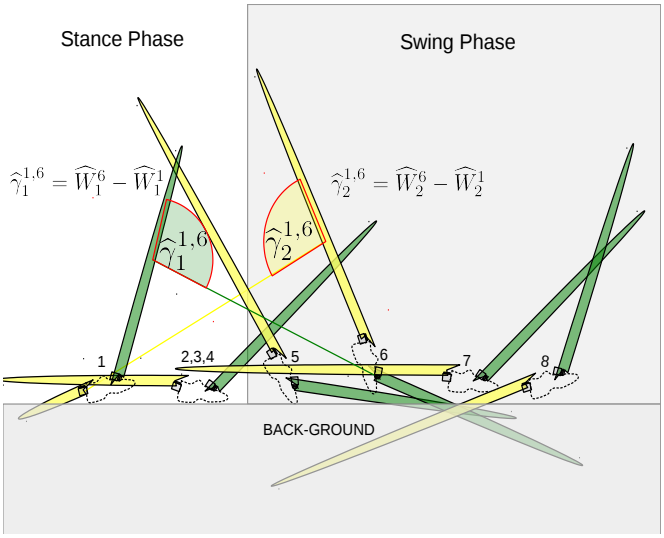


Fig. 3. The Smart Shoe Scanning Field by Gait phase

In Fig. 3, the yellow circle pie is a detected area of the Laser Scanner 2 and the green circle pie is a detected area of the Laser Scanner 1. The 3D space volume covered by the scanning yellow and green color areas is the scanning field of the Smart Shoe moving from the Stance phase to the Swing phase. Otherwise, the gait and positions of this movement can be divided into two phases and 8 positions [20] [22], respectively, such as in Fig. 4. The maximum scanning angle of Laser Scanner 1, $\widehat{\gamma}_1^{1,6}$, and Laser Scanner 2, $\widehat{\gamma}_2^{1,6}$, can be estimated at the position 1 and 6 of the human gait in Fig.4 and Fig. 3.

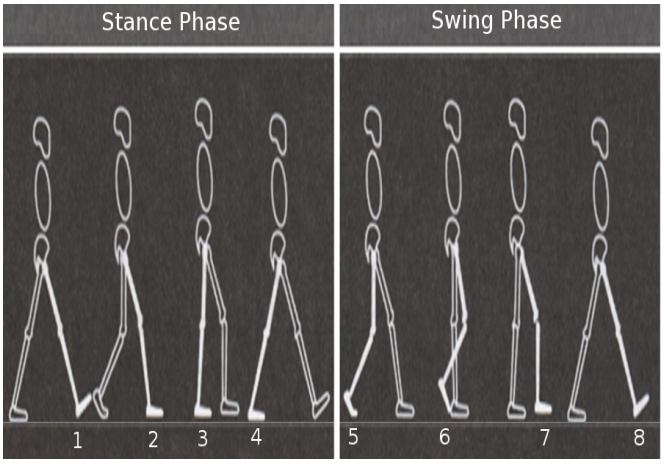


Fig. 4. The Human Motion Gait Phase

However, we usually walk on a flat background, or the real scanning angle composed by both laser scanners 1 and 2 is obtained as:

$$\widehat{\gamma}_{1U}^{1,6} = \widehat{\gamma}_1^{1,6} - \widehat{\gamma}_{1L}^{1,6} \quad (1a)$$

$$\widehat{\gamma}_{2U}^{1,6} = \widehat{\gamma}_2^{1,6} - \widehat{\gamma}_{2L}^{1,6} \quad (1b)$$

$$\widehat{\gamma}_b = \pi - (\widehat{\gamma}_{1U}^{1,6} + \widehat{\gamma}_{2U}^{1,6}), \quad (1c)$$

where $\widehat{\gamma}_{1U}^{1,6}$ is a real scanning angle of Laser Scanner 1 above the background, $\widehat{\gamma}_{2U}^{1,6}$ is a real scanning angle of Laser Scanner 2 above the background, and $\widehat{\gamma}_b$ is un-scanned angle of this Smart Shoe. The estimation value of the un-scanned angle is $\widehat{\gamma}_b$ is $\pi/6 \leq \widehat{\gamma}_b \leq \pi/3$ [20]. We can see intuitively this estimation from Fig. 5.

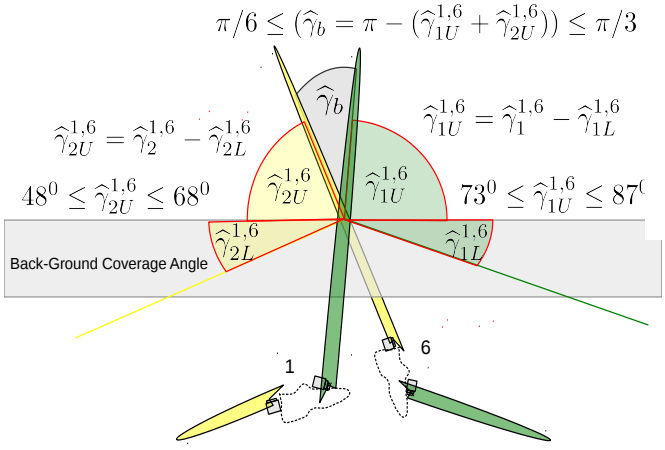


Fig. 5. The Smart Shoe Scanning Field Estimation

Depending on the walking speed, the un-scanned angle of the Smart Shoe can be from $\pi/6$ to $\pi/3$. In the normal walking speed it is about $\pi/4$. However this lacking volume can be compensated by the scanning volume of the next walking step. Hence this design can warranty to scan fully a 3D map of the half sphere of the environment around the human foot motion.

### C. Data Collecting and Processing

Based on the design of the Smart Shoe above, we can definitely calculate the 3D position of any scanning point from laser scanners in their body frame and then transform them into the NED (North East Down) frame [6], [9], [10]. For a general case, we assume in the Smart Shoe is designed so that the Laser Scanner 1's detection area $dA_1^0$ and Laser Scanner 2's detection area $dA_2^0$ are different. The maximum detected distance at any scanning time $t$ of any point $i$ of Laser Scanner 1, $d_1^t(i)$, and that of Laser Scanner 2, $d_2^t(i)$, are different (see Fig. 6 and 7). The number of points for each degree of Laser Scanner 1 and 2 are also different, $nP_1$ and $nP_2$. Hence, the Laser Scanner 1 has total scanning points of a laser scanning field $D_1^{max} * nP_1$ points and $D_2^{max} * nP_2$ points for the Laser Scanner 2. The duration time for a full scan of Laser Scanner 1 is $\delta_1 t$, and Laser Scanner 2 is $\delta_2 t$, $\delta_1 t \neq \delta_2 t$. And the duration time for $IMU$ sensor respondent is $\delta_I t$. Normally $\delta_I t$ is thousand times smaller than $\delta_1 t$ and $\delta_2 t$.

Our target now is to calculate all scanning points returning from each of these laser scanners and then transform them into the NED frame system. We can obtain a 3D cloud points data set of the scanned environment. From this data set, we can calibrate and match them together for building a 3D map.

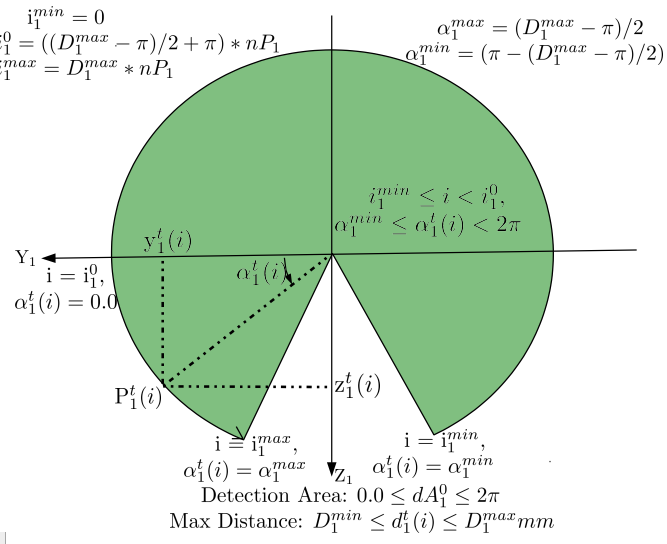


Fig. 6. Laser Scanner 1

*1) Front Laser Scanner 1 Data:* In this sub section, we convert each point getting from Laser Scanner 1 into its 3D body frame such as in Fig. 6. Let $Y_1 O_1 Z_1$ be the coordinate of the body frame of Laser Scanner 1. The 3D coordinate values of any point $i$ at any scanning time $t$ of Laser Scanner 1 can be obtained:

$$x_1^t(i) = 0.0 \tag{2a}$$
$$y_1^t(i) = d_1^t(i) * cos(\alpha_1^t(i)) \tag{2b}$$
$$z_1^t(i) = d_1^t(i) * sin(\alpha_1^t(i)) \tag{2c}$$

Where $\alpha_1^t(i)$ and $i$ are as follows:
$if \quad i_1^{min} \leq i < i_1^0 \quad then \quad \alpha_1^{min} \leq \alpha_1^t(i) < 2\pi$
$if \quad i_1^0 \leq i \leq i_1^{max} \quad then \quad 0.0 \leq \alpha_1^t(i) \leq \alpha_1^{max}$
$i_1^{min} = 0, \quad i_1^0 = ((D_1^{max} - \pi)/2 - \pi) * nP_1,$
$i_1^{max} = D_1^{max} * nP_1$
$\alpha_1^{min} = (\pi - (D_1^{max} - \pi)/2), \quad \alpha_1^0 = 0.0,$
$\alpha_1^{max} = (D_1^{max} - \pi)/2$

Because we designed the $LaserScanner1$ body frame, $IMU$ body frame and $SmartShoe$ body frame equivalently, $O_S \equiv O_1 \equiv O_I$, we can easily transform a 3D point coordinate $(x_1^t(i), y_1^t(i), z_1^t(i))$ of Laser Scanner 1 into the $SmartShoe$ body frame $(x_{1SS}^t(i), y_{1SS}^t(i), z_{1SS}^t(i))$ by:

$$x_{1SS}^t(i) = x_1^t(i) \tag{3a}$$
$$y_{1SS}^t(i) = y_1^t(i) \tag{3b}$$
$$z_{1SS}^t(i) = z_1^t(i) \tag{3c}$$

The index $_{SS}$ in these equations means coordinate value in the $SmartShoe$ body frame. Now we only need to transform one more time this a 3D coordinate value from $SmartShoe$ body frame into the Earth frame, NED as discussed in the subsection II-D.

*2) Rear Laser Scanner 2 Data:* The rear Laser Scanner 2 body frame has a different angle $\widehat{\beta}_{O_1O_2}$ with the other. It has a distance $d_{O_1O_2}$ between its and the Laser Scanner 1's body frame. We can select a segment $O_1O_2$ as $O_2X_2$ axis, $O_2Y_2$ is parallel with $O_1Y_1$, and finally $O_2Z_2$ is a $\widehat{\beta}_{O_1O_2}$ angle different with $O_1Z_1$ such as in Fig. 1. The $LaserScanner2$ body frame is explained in Fig. 7.

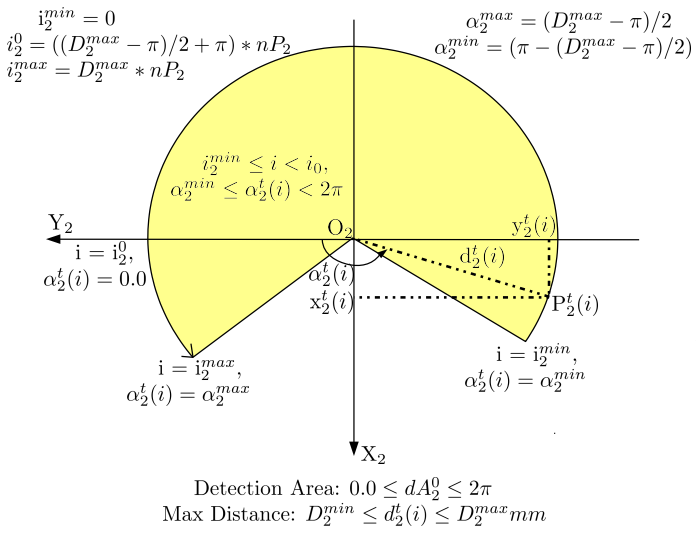


Fig. 7. Laser Scanner 2

Equations converting the distance of any point $i$ in any scanning time $t$ returning from Laser Scanner 2 into a 3D coordinate of $LaserScanner2$ body frame are:

$$x_2^t(i) = d_2^t(i) * sin(\alpha_2^t(i)) \tag{4a}$$
$$y_2^t(i) = d_2^t(i) * cos(\alpha_2^t(i)) \tag{4b}$$
$$z_2^t(i) = 0.0 \tag{4c}$$

Where $\alpha_2^t(i)$ and $i$ are as follows:
$if \quad i_2^{min} \leq i < i_2^0 \quad then \quad \alpha_2^{min} \leq \alpha_2^t(i) < 2\pi$
$if \quad i_2^0 \leq i \leq i_2^{max} \quad then \quad 0.0 \leq \alpha_2^t(i) \leq \alpha_2^{max}$
$i_2^{min} = 0, \quad i_2^0 = ((D_2^{max} - \pi)/2 - \pi) * nP_2,$
$i_2^{max} = D_2^{max} * nP_2$
$\alpha_2^{min} = (\pi - (D_2^{max} - \pi)/2), \quad \alpha_2^0 = 0.0,$
$\alpha_2^{max} = (D_2^{max} - \pi)/2$

Then processing of the rear Laser Scanner 2 data is to transform $(x_2^t(i), y_2^t(i), z_2^t(i))$ in its body coordinate system into the $SmartShoe$ body coordinate system $(x_{2SS}^t(i), y_{2SS}^t(i), z_{2SS}^t(i))$ as:

$$x_{2SS}^t(i) = (x_2^t(i) + d_{O_1O_2}) * cos(\widehat{\beta}_{O_1O_2}) \tag{5a}$$
$$y_{2SS}^t(i) = y_2^t(i) \tag{5b}$$
$$z_{2SS}^t(i) = (x_2^t(i) + d_{O_1O_2}) * sin(\widehat{\beta}_{O_1O_2}) \tag{5c}$$

Where $d_{O_1O_2}$ is the distance between $O_1$ and $O_2$ and $\widehat{\beta}_{O_1O_2}$ is the different angle between segment $O_1O_2$ and axis $O_1X_1$.

### D. Transforming Laser Scanning Data into NED frame

This is an important step to process laser scanning data. Assume that we have a point $\boldsymbol{P}_{SS}^t(i) = (x_{SS}^t(i), y_{SS}^t(i), z_{SS}^t(i))$ in the Smart Shoe body frame, this point is any point $i$ in the data set getting from either Laser Scanner 1 or 2 at a time $t$. We need to transform all points in this data set into the $NED$ frame system. The transformation of any point i at any scanning time $t$ from the $SmartShoe$ data body frame into the $NED$ frame can be obtained as:

$$\boldsymbol{P}_{eSS}^t(i) = \boldsymbol{M}_{NED}^t * \boldsymbol{P}_{SS}^t(i), \tag{6}$$

where $\boldsymbol{M}_{NED}^t = \boldsymbol{M}_{NED}^{t|t}$ is a transformation matrix in Equ. (30) which transforms from the $SmartShoe$ body frame into the $NED$ frame.

## III. Foot Motion Localization for a Smart Shoe

This section presents the foot localization algorithm to enable the 3D mapping. The high accuracy of foot's pose estimation is necessary for matching laser scanning data during walking.

### A. Real-time Human Foot Motion Location Algorithm

The general diagram of the human foot motion localization algorithm can be seen in Fig. 8. The ZVU is applied in the stance phase detection of human gait at time $t$ of the IMU output frequency to estimate the drift error of velocity $\delta \boldsymbol{v}_b^t$ and angular rate $\delta \boldsymbol{w}_b^t$.

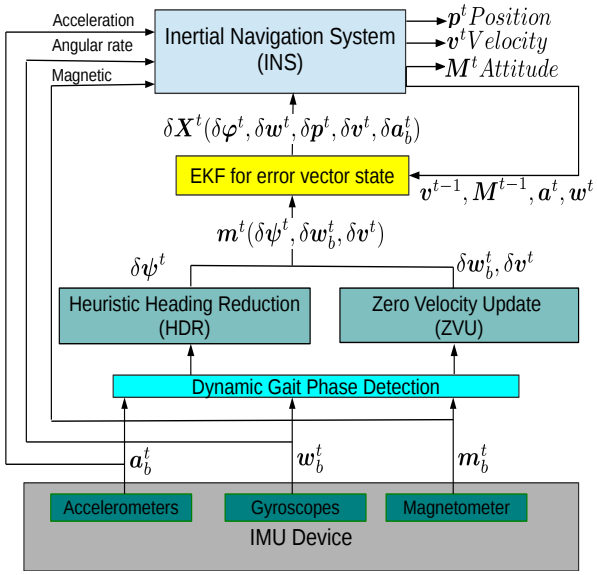


Fig. 8. The general Real-Time INS/EKF ZVU HDR algorithm diagram

$$\delta \boldsymbol{v}_b^t = \boldsymbol{v}_b^t. \tag{7}$$
$$\delta \boldsymbol{w}_b^t = \boldsymbol{w}_b^t. \tag{8}$$

The Heuristic Heading Reduction (HDR) [14] is applied to compute the heading error of foot motion, in $X$ axis or $Yaw$ angle. $\delta\psi^t$ is the drifted $Yaw$ angle of foot motion at time $t$. The drifted errors of the yaw angle $\delta\psi^t$ obtained by HDR, velocity $\delta \boldsymbol{v}_b^t$ and angular rate $\delta \boldsymbol{w}_b^t$ obtained by ZVU form a vector of actual error measurement $\boldsymbol{m}^t$ for the EKF.

$$\boldsymbol{m}^t = (\delta\psi^t, \delta\boldsymbol{w}_b^t, \delta\boldsymbol{v}^t). \tag{9}$$

The output of the EKF estimation at time $t-1$ is a 15 elements error state vector $\delta \boldsymbol{X}^{t-1|t-1}$. This error state vector is used to correct the estimated values of velocity, position, and attitude for the INS module (see Fig. 8).

$$\delta \boldsymbol{X}^{t-1|t-1} = \delta \boldsymbol{X}^{t-1}(\delta\boldsymbol{\varphi}^{t-1}, \delta\boldsymbol{w}^{t-1}, \delta\boldsymbol{p}^{t-1}, \delta\boldsymbol{v}^{t-1}, \delta\boldsymbol{a}_b^{t-1}). \tag{10}$$

where $\delta\boldsymbol{\varphi}^{t-1}$, $\delta\boldsymbol{w}^{t-1}$, $\delta\boldsymbol{p}^{t-1}$, $\delta\boldsymbol{v}^{t-1}$, and $\delta\boldsymbol{a}_b^{t-1}$ represent attitude, angular rate, position, velocity, and acceleration error, respectively. The error state transition of the EKF at time $t$ is obtained:

$$\delta\boldsymbol{X}^{t|t-1} = \boldsymbol{\Phi}^t \delta\boldsymbol{X}^{t-1|t-1} + \boldsymbol{w}_{t-1}. \tag{11}$$

where $\delta\boldsymbol{X}^{t|t-1}$ is the predicted error state at time $t$, $\delta\boldsymbol{X}^{t-1|t-1}$ is the EKF state error at time $t-1$, and $\boldsymbol{w}_{t-1}$ is the process noise with covariance matrix $\boldsymbol{Q}_{t-1} = \boldsymbol{E}(\boldsymbol{w}^{t-1}(\boldsymbol{w}^{t-1})^T)$. The $\boldsymbol{\Phi}^t$ with its size of $15 \times 15$ is defined in Equ. (12).

$$\boldsymbol{\Phi}^t = \begin{bmatrix} \boldsymbol{I} & \boldsymbol{\Phi}^t(01) & \boldsymbol{0} & \boldsymbol{0} & \boldsymbol{0} \\ \boldsymbol{0} & \boldsymbol{I} & \boldsymbol{0} & \boldsymbol{0} & \boldsymbol{0} \\ \boldsymbol{0} & \boldsymbol{0} & \boldsymbol{I} & \boldsymbol{\Phi}^t(23) & \boldsymbol{\Phi}^t(24) \\ \boldsymbol{\Phi}^t(31) & \boldsymbol{0} & \boldsymbol{0} & \boldsymbol{I} & \boldsymbol{\Phi}^t(34) \\ \boldsymbol{0} & \boldsymbol{0} & \boldsymbol{0} & \boldsymbol{0} & \boldsymbol{\Phi}^t(44) \end{bmatrix} \tag{12}$$

where, $\boldsymbol{I}$ is an unit $3 \times 3$ matrix, $\boldsymbol{0}$ is a zero $3 \times 3$ matrix.
$\boldsymbol{\Phi}^t(01) = \Delta(t) \cdot \boldsymbol{M}_{NED}^{t|t-1}, \boldsymbol{\Phi}^t(23) = \Delta(t) \cdot \boldsymbol{I}$
$\boldsymbol{\Phi}^t(31) = -\Delta(t) \cdot \boldsymbol{S}(a_{n'}^t), \boldsymbol{\Phi}^t(34) = \Delta(t) \cdot \boldsymbol{M}_{NED}^{t|t-1}$
$\boldsymbol{\Phi}^t(24) = \dfrac{-\Delta(t)^2}{2} \cdot \boldsymbol{S}(a_{n'}^t), \boldsymbol{\Phi}^t(44) = -\Delta(t) \cdot \boldsymbol{S}(a_{n'}^t)$

The term $\boldsymbol{S}(a_{n'}^t)$ in Equ. (12) is the skew symmetric matrix for accelerations to help the EKF estimate $Roll$ and $Pitch$.

$$\boldsymbol{S}(\boldsymbol{a}_{n'}^t) = \begin{bmatrix} 0 & -\boldsymbol{a}_{n'}^t(2) & \boldsymbol{a}_{n'}^t(1) \\ \boldsymbol{a}_{n'}^t(2) & 0 & -\boldsymbol{a}_{n'}^t(2) \\ -\boldsymbol{a}_{n'}^t(1) & \boldsymbol{a}_{n'}^t(0) & 0 \end{bmatrix} \tag{13}$$

where, $\boldsymbol{a}_{n'}^t$ is the bias-corrected acceleration in the navigation frame or the $NED$ frame.

$$\boldsymbol{a}_{n'}^t = \boldsymbol{M}_{NED}^{t|t-1} \cdot \boldsymbol{a}_{b'}^t \tag{14}$$

where, $\boldsymbol{M}_{NED}^{t|t-1}$ is a transformation matrix defined in Equ. (16). At time $t$ of $IMU$ output data, we get raw value of acceleration and angular rate from $IMU$ in its body frame: $\boldsymbol{a}_b^t$, $\boldsymbol{w}_b^t$, respectively.

We then compute the bias compensation for acceleration $\boldsymbol{a}_{b'}^t$ and angular rate $\boldsymbol{w}_{b'}^t$ from the EKF error state vector $\delta\boldsymbol{X}^{t-1|t-1}$, Equ. (10):

$$\boldsymbol{w}_{b'}^t = \boldsymbol{w}_b^t - \delta\boldsymbol{w}_b^t \tag{15a}$$
$$\boldsymbol{a}_{b'}^t = \boldsymbol{a}_b^t - \delta\boldsymbol{a}_b^t \tag{15b}$$

The transformation matrix $\boldsymbol{M}_{NED}^{t|t-1}$ at time $t$ that transforms the data in the $IMU$ body frame into the navigation frame or the $NED$ frame:

$$\boldsymbol{M}_{NED}^{t|t-1} = \boldsymbol{M}_{NED}^{t-1|t-1} \cdot \frac{2\boldsymbol{I}_{3\times3} + \delta\boldsymbol{\Omega}_{t-1} \cdot \Delta(t)}{2\boldsymbol{I}_{3\times3} - \delta\boldsymbol{\Omega}_{t-1} \cdot \Delta(t)}, \tag{16}$$

where, $\delta\boldsymbol{\Omega}_{t-1}$ is skew symmetric matrix for angular rate:

$$\delta\boldsymbol{\Omega}_{t-1} = \begin{bmatrix} \boldsymbol{0} & -\boldsymbol{w}_{b'}^{t-1}(2) & \boldsymbol{w}_{b'}^{t-1}(1) \\ \boldsymbol{w}_{b'}^{t-1}(2) & \boldsymbol{0} & -\boldsymbol{w}_{b'}^{t-1}(0) \\ -\boldsymbol{w}_{b'}^{t-1}(1) & \boldsymbol{w}_{b'}^{t-1}(0) & \boldsymbol{0} \end{bmatrix} \tag{17}$$

where, $\boldsymbol{w}_{b'}^{t-1}$ computed by Equ. (15a), $\boldsymbol{M}_{NED}^{t-1|t-1}$ is the last rotation matrix updated by the EKF at the previous step $t-1$. At the first time $t$ = 1, we can estimate the $\boldsymbol{M}_{NED}^{1|0}$ as

$$\boldsymbol{M}_{NED}^{1|0} = \begin{bmatrix} \boldsymbol{M}_{00} & \boldsymbol{M}_{01} & \boldsymbol{M}_{02} \\ \boldsymbol{M}_{10} & \boldsymbol{M}_{11} & \boldsymbol{M}_{12} \\ \boldsymbol{M}_{20} & \boldsymbol{M}_{21} & \boldsymbol{M}_{22} \end{bmatrix} \tag{18}$$

where, $\boldsymbol{M}_{00} = c(\gamma)c(\beta), \boldsymbol{M}_{01} = c(\gamma)s(\alpha)s(\beta) - c(\alpha)s(\gamma)$,
$\boldsymbol{M}_{02} = s(\alpha)s(\gamma) + c(\alpha)c(\gamma)s(\beta), \boldsymbol{M}_{10} = c(\beta)s(\gamma)$,
$\boldsymbol{M}_{11} = c(\alpha)c(\gamma) + s(\alpha)s(\gamma)s(\beta), \boldsymbol{M}_{12} = c(\alpha)s(\gamma)s(\beta) - c(\gamma)s(\alpha), \boldsymbol{M}_{20} = -s(\beta), \boldsymbol{M}_{21} = c(\beta)s(\alpha), \boldsymbol{M}_{22} = c(\alpha)c(\beta)$. Here, $c$ and $s$ are $cosine()$, $sine()$ functions, respectively, and $\alpha$, $\beta$, and $\gamma$ are roll, pitch and yaw angles of the foot, respectively [14].

The EKF error state at time $t$ can be obtained by

$$\delta\boldsymbol{X}^{t|t} = \delta\boldsymbol{X}^{t|t-1} + \boldsymbol{K}^t \cdot [\boldsymbol{m}^t - \boldsymbol{H}\delta\boldsymbol{X}^{t|t-1}] \tag{19}$$

where, $\boldsymbol{K}_{t-1}$ is the Kalman gain defined in Equ. (22); $\boldsymbol{m}^t$ is defined in Equ. (9) and $\boldsymbol{H}$ is a measurement matrix:

$$\boldsymbol{H}_{7\times15} = \begin{bmatrix} \boldsymbol{O}_{1\times3}^1 & \boldsymbol{O}_{1\times3}^0 & \boldsymbol{O}_{1\times3}^0 & \boldsymbol{O}_{1\times3}^0 & \boldsymbol{O}_{1\times3}^0 \\ \boldsymbol{O}_{3\times3} & \boldsymbol{I}_{3\times3} & \boldsymbol{O}_{3\times3} & \boldsymbol{O}_{3\times3} & \boldsymbol{O}_{3\times3} \\ \boldsymbol{O}_{3\times3} & \boldsymbol{O}_{3\times3} & \boldsymbol{O}_{3\times3} & \boldsymbol{I}_{3\times3} & \boldsymbol{O}_{3\times3} \end{bmatrix} \tag{20}$$

where, $\boldsymbol{O}_{1\times3}^1$ = [0 0 1], $\boldsymbol{O}_{1\times3}^0$ = [0 0 0], $\boldsymbol{I}3 \times 3$ is a $3 \times 3$ unit matrix, and $\boldsymbol{O}_{3\times3}$ is a $3 \times 3$ zero matrix.
The measurement model of the EKF is defined as

$$\boldsymbol{z}^t = \boldsymbol{H}\delta\boldsymbol{X}^{t|t} + \boldsymbol{n}^t \tag{21}$$

where, $\boldsymbol{n}^t$ is the measurement noise with covariance matrix $\boldsymbol{R}^t = \boldsymbol{E}(\boldsymbol{n}^t(\boldsymbol{n}^t)^T)$.

The Kalman gain is obtained by

$$\boldsymbol{K}^t = \boldsymbol{P}^{t|t-1}\boldsymbol{H}^T(\boldsymbol{H}\boldsymbol{P}^{t|t-1}\boldsymbol{H}^T + \boldsymbol{R}^t)^{-1}, \tag{22}$$

where $\boldsymbol{P}^{t|t-1}$ is the estimation error covariance matrix which is computed at times $t$ of $IMU$ output consequence:

$$\boldsymbol{P}^{t|t-1} = \Phi^{t-1}\boldsymbol{P}^{t-1|t-1}(\Phi^{t-1})^T + \boldsymbol{Q}^{t-1} \tag{23}$$

where, the previous $\boldsymbol{P}^{t-1|t-1}$ is computed by the Kalman gain at time $t-1$ in Equ. (24):

$$\boldsymbol{P}^{t-1|t-1} = (\boldsymbol{I} - \boldsymbol{K}^{t-1}\boldsymbol{H})\boldsymbol{P}^{t-1|t-2}(\boldsymbol{I} - \boldsymbol{K}^{t-1}\boldsymbol{H})^T \tag{24}$$

where, $\boldsymbol{I}$ is unit $15 \times 15$ matrix. Now we can compute the acceleration $\boldsymbol{a}_e^t$ of human motion in the $NED$ frame by converting the bias-compensated acceleration from Equ. (15b) to earth navigation frame $NED$ then subtracting the gravity acceleration vector $\boldsymbol{g}_e$ = $(0.0, 0.0, 9.8m/s^2)$:

$$\boldsymbol{a}_e^t = \boldsymbol{M}_{NED}^{t|t-1} \cdot \boldsymbol{a}_{b'}^t - \boldsymbol{g}_e. \tag{25}$$

Then the velocity in earth $NED$ frame prior the EKF correction at time $t$ is obtained by integrating the acceleration between two consequence outputs of IMU:

$$\boldsymbol{v}^{t|t-1} = \boldsymbol{v}^{t-1|t-1} + \boldsymbol{a}_e^t \cdot \Delta(t). \tag{26}$$

This velocity is integrated one more time to compute the foot position in Earth navigation frame:

$$\boldsymbol{p}^{t|t-1} = \boldsymbol{p}^{t-1|t-1} + \boldsymbol{v}^{t|t-1} \cdot \Delta(t). \tag{27}$$

Finally, we apply the error state vector from EKF in Equ. (19) to correct the values of velocity in Equ. (26), position in Equ. (27), and attitude in Equ. (16).

$$\boldsymbol{v}^{t|t} = \boldsymbol{v}^{t|t-1} - \delta\boldsymbol{v}^{t|t} \tag{28}$$

$$\boldsymbol{p}^{t|t} = \boldsymbol{p}^{t|t-1} - \delta\boldsymbol{p}^{t|t} \tag{29}$$

$$\boldsymbol{M}_{NED}^{t|t} = \frac{2\boldsymbol{I}_{3\times3} + \delta\boldsymbol{\Theta}_{t-1}}{2\boldsymbol{I}_{3\times3} - \delta\boldsymbol{\Theta}_{t-1}} \cdot \boldsymbol{M}_{NED}^{t|t-1} \tag{30}$$

where:

$$\delta\boldsymbol{\Theta}^{t-1} = -\begin{bmatrix} 0 & -\delta\boldsymbol{\varphi}^{t-1}(2) & \delta\boldsymbol{\varphi}^{t-1}(1) \\ \delta\boldsymbol{\varphi}^{t-1}(2) & 0 & -\delta\boldsymbol{\varphi}^{t-1}(0) \\ -\delta\boldsymbol{\varphi}^{t-1}(1) & \delta\boldsymbol{\varphi}^{t-1}(0) & 0 \end{bmatrix} \tag{31}$$

where, $\delta\boldsymbol{\varphi}^{t-1}$ is the EKF error state for attitude at previous time $t-1$ obtained by Equ. (19).

### B. Calibrating Laser Data with Foot Motion Trajectory

Laser data point $\boldsymbol{P}_{eSS}^{t}(i)$ in the $NED$ system should be calibrated with the foot motion trajectory so that we can obtain a correct map of the environment. Because the $SmartShoe$ body frame centered at $O_S$ is equivalent to the $IMU$ body frame centered at $O_I$, the trajectory of foot motion based on the movement of $SmartShoe$ rigid body system $O_S$ is equivalent to $O_I$. This also means that the real-time position of $O_I$ or trajectory of foot movement is the root for every laser point $\boldsymbol{P}_{eSS}^{t}(i)$ in a 3D map. Hence we can compute the real-time position of all 3D mapping points of the surrounding environment along with the foot movement $\boldsymbol{P}_{NED3D}^{t}(i)$:

$$\boldsymbol{P}_{NED3D}^{t}(i) = \boldsymbol{P}_{eSS}^{t}(i) + \boldsymbol{p}^{t} \tag{32}$$

where, the $\boldsymbol{p}^t = \boldsymbol{p}^{t|t}$ is a 3D position on the human foot motion trajectory at time $t$ in the $NED$ frame.

## IV. Real-time 3D Mapping Algorithm

The real-time 3D mapping algorithm is presented in Fig. 9. The algorithm designed based on ROS (Robotic Operating System) [16] starting by the Start event to mount Laser Scanner 1, 2 and IMU sensor. The result of this event is three new Listener nodes: $L_2-Listener, L_1-Listener$ and $I-Listener$ for Laser Scanner 1, 2 and $IMU$, respectively. Each of them operates independently and parallel each other.

Because their output rate data is different, the waiting time $\delta_1^t, \delta_2^t$, and $\delta_I^t$ are different. Whenever these devices finish their collecting data phase, they make an interruption for their Listener nodes. Then these agents describe the collected data to other modules waiting for processing this data.

In this diagram, Comp $\boldsymbol{P}_2^t(i), \boldsymbol{P}_1^t(i)$ and EKF INS $\boldsymbol{p}^t$ are the processing modules. The modules $\boldsymbol{P}_2^t(i)$ and $\boldsymbol{P}_1^t(i)$ process the stream data from Laser Scanner 1 and 2 , respectively. They convert the distant point $i$ in the scanning data at time $t$ into the 3D coordinate data in the Smart Shoe body frame by the Equ. (2), (3), (4), and (5). Then, the module $\boldsymbol{P}_{eSS}^{t}(i)$ transforms this data from Smart Shoe body frame into the Earth NED system by the Equ. (6).

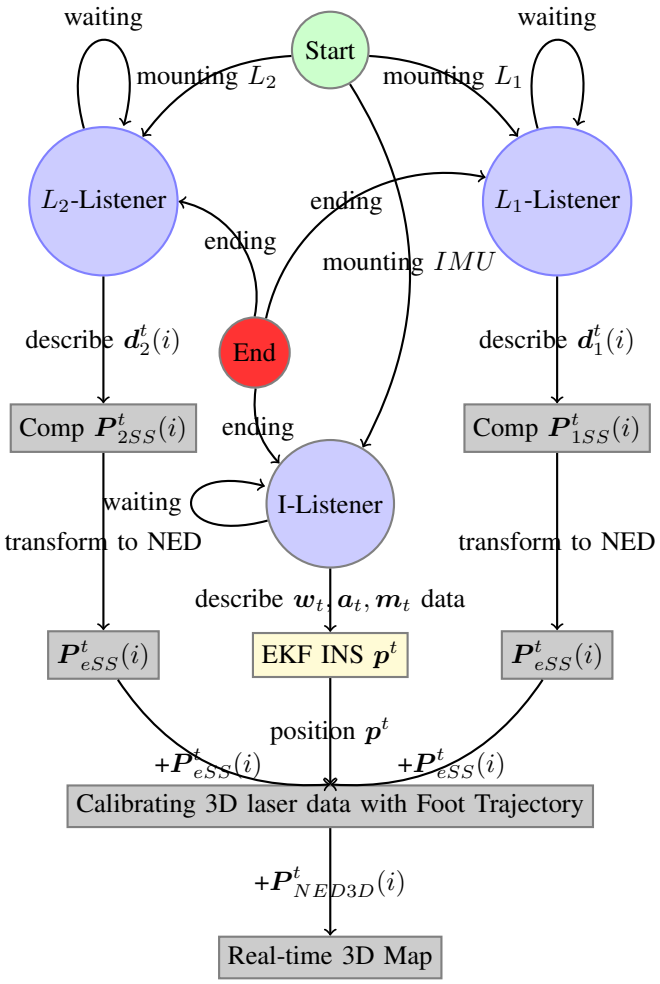


Fig. 9. A Real-time 3D Mapping Algorithm

The $I-Listener$ node of IMU sensor gets the stream data from IMU and then describe it to EKF INS $\boldsymbol{p}^t$ module. This module bases on the acceleration, angle rate, and magnetic data from IMU description to integrate the velocity, position of foot motion in a very small respondent duration time of IMU to I-Listener. This process is supported by the EKF filter presented in the previous section. The EKF INS filter helps minimize accumulated errors from IMU drift by time. This EKF INS $\boldsymbol{p}^t$ module outputs an accurate trajectory data of foot motion.

The module "Calibrating 3D laser data with Foot Trajectory" processes the calibration of the foot trajectory data with 3D laser data to build a 3D map of the environment.

## V. Experimental Results

We implemented the design of the Smart Shoe in Fig. 1 on a Puma sport shoe with a white soft ring around it's header as shown in Fig. 10. On the white soft ring, we attached two Hokuyo URG-04LX-UG01 laser scanners and one MicroStrain 3DM-GX3-25 IMU sensor.

The design and implementation of the white soft ring follows all requirements of the Smart Shoe design in Fig. 1. Namely, Hokuyo 1 is attached on the Laser Scanner 1 position, and Hokuyo 2 is attached on the Laser Scanner 2 position, and MicroStrain 3DM-GX3-25 IMU is attached


Fig. 10. A Smart Shoe implementation

under the Hokuyo 1.

The white soft ring in this implementation is tight on the shoe by the shoe string. This white soft ring has two important roles. It is hard enough to be able to attach all devices on the shoe tightly. But it also warranties the required designing angle between Hokuyo 2 body frame and Smart Shoe body frame. The white soft ring here also makes Smart Shoe light and comfortable for wearing and it can be unplugged from the shoe easily. All integrated devices can be connected with a computer by USB cables.

Two Hokuyo laser scanners in this implementation have identical technical specifications: the detection area $D_1^{max}, D_2^{max}$ is $240^0$, the number of scanning points $nP_1, nP_2$ for each degree of scanning detection area is approximated 3 points, and the maximum detection distance $d_1^t(i), d_2^t(i)$ is less than or equal to 4,000 $mm$. Time of a full scan of $240^0$ is nearly 0.8 $s$. The distance $d_{O_1O_2}$ is 0.22 $m$. The different angle $\widehat{\beta}_{O_1O_2}$ is $\pi/6$.

All collected data is processed by the proposed real-time mapping algorithm as presented in Fig. 9. It is coded by C++ language and runs on the Hydro ROS (Robotic Operating System) platform. We tested our Smart Shoe inside the $3^{rd}$ floor in the Scrugham Engineering and Mines (SEM) building, University of Nevada, Reno (UNR) campus. The speed of walking was different: normal, slow, fast and very fast. The Smart Shoe collected more than 3 millions of 3D points for this hallway and the size of raw data set for one time collection is over 135Mb data.

Fig. 11 presents a 3D mapping result of the SEM hallway. Namely, Fig. 11 (1) is the trajectories of the foot with normal walking speed (about 1.28 m/s) plotted on the 2D floor plan of the $3^{rd}$ of the SEM building. We can see that the accuracy of the human localization with IMU is very high since the starting and ending location are very close together, and the trajectory matches with the floor plan. Fig. 11 (2) is the online 3D map of the hallway created by the proposed Smart Shoe during the walking. The Fig. 11 (3) (a),(b),(c), and (d) are zoom-in maps at some locations of the 3D map in Fig. 11 (2) to intuitively shown the quality of the 3D scanning map by the proposed Smart Shoe.

## VI. Conclusion and Future Work

This paper proposed a new comfortable wearing device, Smart Shoe, for building a real-time 3D map of the surrounding environment. By wearing this shoe the user can normally work and build the map simultaneously. The overall design of the shoe with details of sensor integration, data collection, transformation and processing was reported. The human foot localization algorithm was proposed to accurately track and localize the foot motion for matching laser scanning data. The 3D real-time mapping algorithm was introduced to allows the user to build a map of the environments. Experimental results of the foot motion localization and 3D mapping are conducted to demonstrated the proposed approaches.

## References

[1] Velodyne lidar available. *http://www.velodynelidar.com/lidar/lidar.aspx*, 2014.

[2] Dorit Borrmann, Andreas Nchter, Marija akulovi, Ivan Maurovi, Ivan Petrovi, Dinko Osmankovi, and Jasmin Velagi. A mobile robot based system for fully automated thermal 3d mapping. *Advanced Engineering Informatics*, 28(4):425 – 440, 2014.

[3] Z. J. Chong, B. Qin, T. Bandyopadhyay, M. H. Ang Jr., E. Frazzoli, and D. Rus. Synthetic 2d lidar for precise vehicle localization in 3d urban environment. *IEEE International Conference on Robotics and Automation (ICRA)*, pages 1554–1559, May 2013.

[4] G. Cai et al. Unmanned rotorcraft systems. *Advances in Industrial Control, Springer-Verlag London Limited*, pages 2657–2666, 2011.

[5] P. Fritzson. *Principles of Object-Oriented Modeling and Simulation with Modelica 2.1*. IEEE Press, US, 2004.

[6] W. George and II. Collins. *The Foundations of Celestial Mechanics*. The Pachart Foundation dba Pachart Publishing House and reprinted by permission, US, 2004.

[7] V.M. Hernandez Bennetts, A.J. Lilienthal, A.A. Khaliq, V. Pomareda Sese, and M. Trincavelli. Towards real-world gas distribution mapping and leak localization using a mobile robot with 3d and remote gas sensing capabilities. In *Robotics and Automation (ICRA), 2013 IEEE International Conference on*, pages 2335–2340, May 2013.

[8] Skog I., Handel P., Nilsson J., and J. Rantakokko. Zero-velocity detectionan algorithm evaluation. *Biomedical Engineering, IEEE Transactions*, 57(11):2657–2666, November 2010.

[9] R. S. Lim, H. M. La, and W. Sheng. A robotic crack inspection and mapping system for bridge deck maintenance. *Automation Science and Engineering, IEEE Transactions*, 11(2):367–378, April 2014.

[10] R.S. Lim, H. M. La, Z. Shan, and W. Sheng. Developing a crack inspection robot for bridge maintenance. In *Robotics and Automation (ICRA), 2011 IEEE International Conference on*, pages 6288–6293, May 2011.

[11] P. Moghadam, M. Bosse, , and R. Zlot. Line-based extrinsic calibration of range and image sensors. *Robotics and Automation (ICRA), 2013 IEEE International Conference on*, pages 3685–3691, May 2013.

[12] M. P. Murray, L. A. Mollinger, G. M. Gardner, and S. B. Sepic. Kinematic and emg patterns during slow free and fast walking. *Orthopaedic Research*, 2:272–280, 1984.

[13] Andreas Nchter, Kai Lingemann, Joachim Hertzberg, and Hartmut Surmann. 6d slam3d mapping outdoor environments. *Journal of Field Robotics*, 24(8-9):699–722, 2007.

[14] L. V. Nguyen, H. M. La, and T. H. Duong. Dynamic human gait phase detection algorithm. *Proc. of The ISSAT International Conference on Modeling of Complex Systems and Environments (MCSE)*, 2015.

[15] S. Song and H. Geyer. Regulating speed and generating large speed transitions in a neuromuscular human walking model. *IEEE International Conference on Robotics and Automation*, May 2012.

[16] Robot Operating System. Ros hydro. *http://www.ros.org/*, 2015.

[17] S. Thrun, W. Burgard, and D. Fox. A real-time algorithm for mobile robot mapping with applications to multi-robot and 3d mapping. In *Robotics and Automation, 2000. Proceedings. ICRA '00. IEEE International Conference on*, volume 1, pages 321–328 vol.1, 2000.

[18] E. Turner, P. Cheng, and A. Zakhor. Fast, automated, scalable generation of textured 3d models of indoor environments. *submitted to IEEE Journal on Selected Topics in Signal Processing*, 2014.

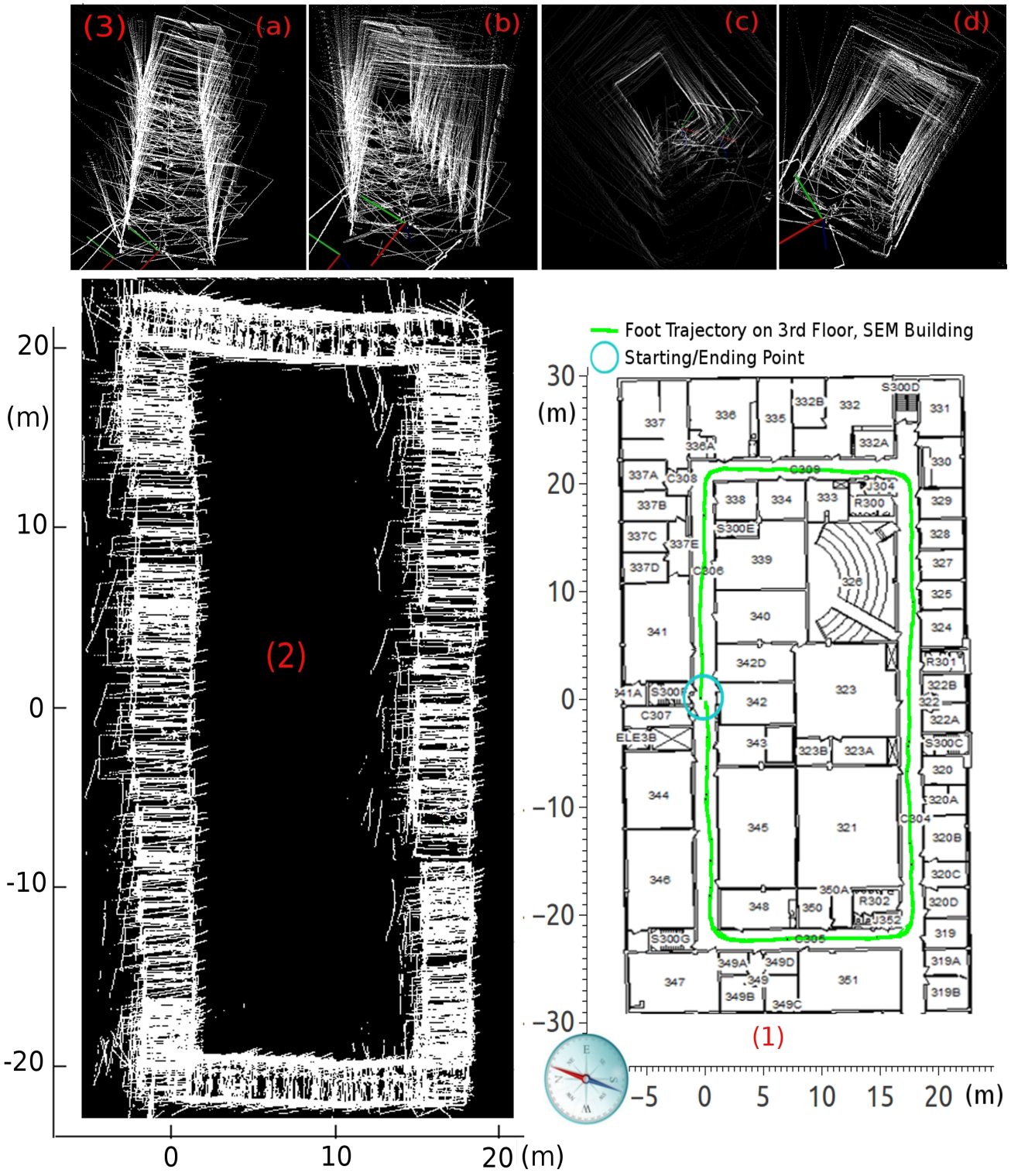


Fig. 11. The 3D mapping result of the $3^{rd}$ floor hallway in the SEM building at the University of Nevada at Reno (UNR) campus: (1) Trajectory of the human foot during normal walking (1.28 m/s) along the hallway while wearing the proposed Smart Shoe for 3D map building; (2) The result of 3D map construction of the hallway, and (3) Zoom-in at some locations of the hallway map.


[19] X. Yun, Calusdian, J. Bachmann, E.R. McGhee, and R.B. McGhee. Estimation of human foot motion during normal walking using inertial and magnetic sensor measurements. *Instrumentation and Measurement, IEEE Transactions*, 61(7):2059–2072, July 2012.

[20] H. Zhang, J. Qian, L. Shen, and Y. Zhang. Research on healthy subject gait cycle phase at different walking speeds. *Robotics and Biomimetics (ROBIO), 2012 IEEE International Conference on*, pages 1349–1354, December 2012.

[21] J. Zhang and S. Singh. Loam: Lidar odometry and mapping in real-time. *Robotics: Science and Systems Conference (RSS)*, 2014.

[22] R. Zhang, C. Vogler, and D. Metaxas. Human gait recognition. *Computer Vision and Pattern Recognition Workshop, 2004. CVPRW '04. Conference on*, pages 18–18, Jun 2004.